Magnetic anisotropy of Fe and Co adatoms and Fe clusters magnetically decoupled from $Ni_3Al(111)$ by an alumina bilayer

A. Lehnert,[1] S. Rusponi,[1] M. Etzkorn,[1] S. Ouazi,[1] P. Thakur,[2] and H. Brune[1]
[1]*Institute of Condensed Matter Physics, Ecole Polytechnique Fédérale de Lausanne (EPFL), CH-1015 Lausanne, Switzerland*
[2]*European Synchrotron Radiation Facility, Boîte Postale 200, F-38043 Grenoble, France*
(Received 6 August 2009; revised manuscript received 24 November 2009; published 31 March 2010)

The magnetic properties of individual Fe and Co atoms as well as of small Fe clusters adsorbed on two atomic layers of Al_2O_3 grown on $Ni_3Al(111)$ have been investigated by x-ray absorption spectroscopy and x-ray magnetic circular dichroism. We find ratios of the orbital over the effective spin magnetic moments of $r=0.53\pm0.09$ for Fe and $r=0.91\pm0.06$ for Co, which are both very close to the free-atom values of $r=0.5$ and 1, respectively. The magnetization curves acquired at the Fe and Ni edges demonstrate a distinctly different magnetization reversal of the transition-metal nanostructures and the substrate excluding magnetic dipolar or exchange coupling through the alumina film. Our data reveal an out-of-plane easy magnetization axis for Fe and Co originating from the spatially anisotropic hybridization of the 3*d* states of the adatom, with the 2*p* states of the oxygen terminated Al_2O_3 surface. We conclude that the alumina film effectively decouples the magnetic adatoms from the underlying metal substrate while providing a crystal-field environment giving rise to high magnetic anisotropy.

DOI: 10.1103/PhysRevB.81.104430 PACS number(s): 75.75.−c, 75.30.Gw, 78.70.Dm, 68.43.Tj

I. INTRODUCTION

The magnetic properties of surface supported nanometer-scale structures, such as single atoms and small clusters, are of fundamental interest and may possibly play a role in future technological applications such as classical information storage or quantum information processing. The spin (S) and orbital (L) magnetic moments, as well as the magnetic anisotropy energy (MAE) of adatoms and clusters strongly depend on the electronic coupling to the underlaying substrate. For example, a giant MAE has been observed for single Co atoms on Pt(111), as a consequence of the 3*d*(Co)-5*d*(Pt) hybridization combined with a large spin-orbit coupling of the substrate's *d* electrons[1] while vanishing MAE values and atomic like orbital moments have been observed for single Co atoms when deposited on alkali metals where only 3*d*-*sp* hybridization is possible.[2]

Of particular interest are 3*d* transition-metal nanostructures adsorbed on ultrathin insulating films comprising only a few atomic layers. These insulating films may be considered as a spacer that reduces or even suppresses the electronic coupling between the nanoparticles and an underlaying metallic substrate. A recent example is the collective quantum behavior observed in Mn chains on a single CuN layer grown on Cu(100).[3] Moreover, the electronic hybridization with the atoms of the insulating film may result in strongly directional bonding giving rise to a very large MAE as recently reported for single Fe and Co atoms, again on CuN/Cu(100).[4–6] These two aspects make 3*d* transition-metal nanostructures on an ultrathin insulating film a model system for future logic units in atomic scale spintronics.

Here we focus on single atoms and small clusters of Fe and Co adsorbed on a two-atomic-layer-thick Al_2O_3 film grown on $Ni_3Al(111)$. We find that the ratios of the orbital over the effective spin magnetic moment $r=L/(S+7D)$ of $r=0.53\pm0.09$ for Fe and $r=0.91\pm0.06$ for Co are very close to the free-atom values of $r=0.5$ for $3d^6$ (Fe) and $r=1$ for $3d^7$ (Co). Comparison of the magnetization curves acquired at the Fe and Ni edges demonstrates a distinctly different switching behavior for the transition-metal nanostructures and the substrate excluding strong dipolar or exchange coupling. Altogether, these findings demonstrate that the alumina film, despite its thickness of only two atomic layers,[7–9] gives rise to an effective decoupling of the magnetic atoms from the conduction electrons of the underlying metal, as expected by the large band gap of 7–8 eV observed for the present system.[10] Our data reveal an out-of-plane easy magnetization axis for Fe and Co. According to measurements with linearly polarized x rays this perpendicular MAE is a a consequence of a spatially anisotropic hybridization of the 3*d* states of Fe (Co) with the 2*p* states of the oxygen terminated Al_2O_3 surface.

II. EXPERIMENT

The $Ni_3Al(111)$ single crystal was prepared by Ar^+-ion sputtering at room temperature for 30 min ($p_{Ar}=5\times10^{-6}$ mbar, 1 keV) and annealing for 10 min at 960 ± 30 K, reading the temperature with a pyrometer. The alumina thin film has been grown by exposing the clean and ordered $Ni_3Al(111)$ surface during 1 h to oxygen ($p_{O_2}=1\times10^{-7}$ mbar) at 960 ± 30 K and keeping it for one more hour at this temperature without further exposure to O_2. Fe and Co were deposited at $T=10$ K and $p_{tot}<1\times10^{-10}$ mbar by atomic beam epitaxy from high-purity rods (99.995%) using a commercial e-beam evaporator. The flux was typically about 10^{-3} ML/s [1 ML is defined as the atomic density of 1 $Ni_3Al(111)$ plane]. The magnetic properties of the $Al_2O_3/Ni_3Al(111)$ substrate, as well as of the Fe and Co adatoms were investigated by means of x-ray absorption spectroscopy (XAS) and x-ray magnetic circular dichroism (XMCD) at the ID08 beamline of the European Synchrotron-Radiation Facility (ESRF) in Grenoble. XAS

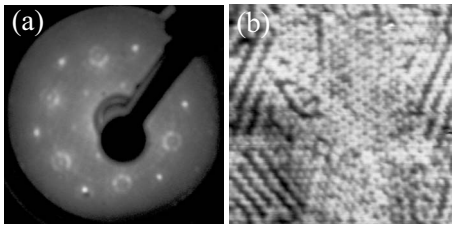

FIG. 1. Al_2O_3 surface oxide on $Ni_3Al(111)$ prepared at 960 ± 30 K and measured at 300 K. (a) LEED pattern obtained at $E=62$ eV and (b) STM image (430 Å$\times$430 Å, $V_t=3.0$ V, $I_t=200$ pA).

experiments were performed in the total electron yield (TEY) mode using $(99\pm1)\%$ circularly polarized light and a ±5 T magnetic field generated by a split coil superconducting magnet. A sketch of the sample position with respect to the field and x-ray beam can be found in Fig. 3(a). The x-ray beam and magnetic field are parallel to each other and form an angle θ with the surface normal of the sample. The out-of-plane vs in-plane magnetization was investigated by rotating the sample from $\theta=0°$ to $\theta=70°$, corresponding to normal and grazing incidence of the x-ray beam, respectively. The coverage calibration has been carried out by XAS and scanning tunneling microscopy (STM).

III. SUBSTRATE CHARACTERIZATION

A. Structural results from LEED and STM

Figure 1(a) shows a low-energy electron-diffraction (LEED) pattern of the $Al_2O_3/Ni_3Al(111)$ surface. We find the characteristic 2×2 spots of the chemically ordered alloy substrate and satellites caused by the oxide superstructure. The LEED pattern resembles the one displayed in Fig. 5 of Ref. 11 which has been interpreted by the authors as two domains of γ'-Al_2O_3 in accordance with high-resolution electron-energy-loss spectroscopy.

The STM image shown in Fig. 1(b) reveals the coexistence of the $(\sqrt{67}\times\sqrt{67})R12.2°$ structure visible in the center of image and different rotational domains of a recently reported *stripe* phase.[9,12] The apparent height differences in the STM image are with 1.0 ± 0.2 Å in agreement with former publications.[13,14] While the $(\sqrt{67}\times\sqrt{67})R12.2°$ structure has holes at the corners of its unit cell[9] the stripe phase is an atomically flat layer. For the present adsorbates Fe and Co, the holes do not get filled, presumably due to a step edge barrier surrounding them.[9] Therefore the Al_2O_3 film used for the present study perfectly separates the metal atoms from the underlying $Ni_3Al(111)$ crystal.

Schmid *et al.*[9] suggest that variations in the stoichiometry of the $Ni_3Al(111)$ crystal may be the origin of the coexistence of different oxide phases. However, we were able to produce a highly ordered alumina film exclusively exhibiting the $(\sqrt{67}\times\sqrt{67})R12.2°$ phase with the very same $Ni_3Al(111)$ crystal as the one used for the measurements in Fig. 1.[13] We therefore conclude that postannealing at 1050 K is essential in order to produce an alumina film with only the $(\sqrt{67}\times\sqrt{67})R12.2°$ structure.[10,11,15] The resistive heater of the preparation chamber at the ESRF did not allow heating to $T=1050$ K. However, as outlined above the Al_2O_3 film obtained with the lower annealing temperature formed a continuous two-atomic-layer-thick and stoichiometric Al_2O_3 film.

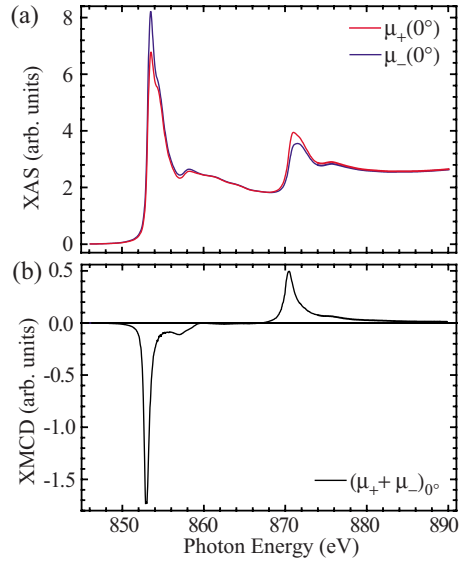

FIG. 2. (Color online) (a) XAS and (b) XMCD of Al_2O_3 surface oxide on $Ni_3Al(111)$ prepared at 960 ± 30 K measured with circularly polarized light at the Ni $L_{2,3}$ edges at $\mu_0H=2$ T and $T=8$ K.

B. Magnetic properties of $Al_2O_3/Ni_3Al(111)$

Earlier measurements of bulk Ni_3Al report a weak itinerant ferromagnetism with a Curie temperature of $T_C=40$ K and a very small magnetic moment of $0.23\mu_B$ per Ni_3Al unit cell.[16,17] Assuming that only the Ni atoms within the cell carry a magnetic moment, $0.077\mu_B$/Ni atom is obtained. In Fig. 2(a) the absorption spectra with circularly polarized light taken at the Ni $L_{2,3}$ edges of the saturated sample are shown. Application of the XMCD sum rules allows to extract independently the orbital magnetic moment L and the effective spin moment $S_{eff}=S+7D$, where S is the spin moment and D the spin dipole moment.[18–20] Using the number of d holes of bulk Ni $h_d=1.66$ (Ref. 21) we obtain $L=0.047\mu_B$/Ni atom and $S=0.357\mu_B$/Ni atom when neglecting the dipolar term. This is smaller than the magnetic moment of bulk Ni of $0.62\mu_B$/atom (Ref. 22) but substantially larger than the above-mentioned magnetic moment of bulk Ni_3Al. This can be explained by a compositional change in the uppermost substrate layers due to the formation of the surface Al_2O_3 layer. The topmost layer of stoichiometric $Ni_3Al(111)$ contains only 25% Al which is not sufficient to form a double layer of alumina. Part of the Al must therefore segregate to the surface from deeper layers resulting in several Ni-rich layers at the interface. This model was confirmed by x-ray photoelectron spectroscopy finding up to 100% Ni in the atomic layers close to the interface with the oxide.[8] The probing depth of x-ray absorption spectroscopy in the

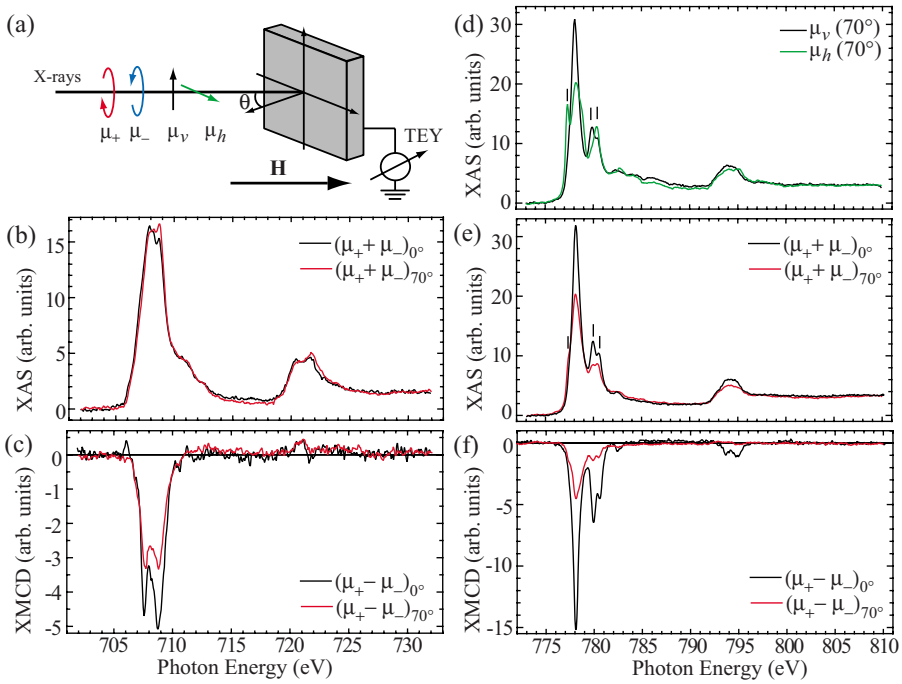

FIG. 3. (Color online) (a) Sketch of the experimental geometry. The incoming x-ray beam is parallel to the applied field **H**. [(b) and (c)] 0.03 ML $Fe/Al_2O_3/Ni_3Al(111)$: total XAS and XMCD spectra taken at the Fe $L_{2,3}$ edges at $T=8$ K and $\mu_0 H=5$ T with circularly polarized light. The spectra at $\theta=70°$ have been normalized to the $\int_{L_3}(\mu_+ + \mu_-)$ intensity at 0° to eliminate the dependence of the electron yield on the sample orientation. The background was subtracted. [(d)–(f)] 0.02 ML $Co/Al_2O_3/Ni_3Al(111)$: (d) XAS taken at Co $L_{2,3}$ edges at $T=8$ K and $\mu_0 H=5$ T with linearly polarized light. [(e) and (f)] Total XAS and XMCD spectra. The data were normalized and background corrected as for (b) and (c). For the μ_+ and μ_- spectra see Ref. 51.

TEY mode is limited to a few nanometers implying that most of the Ni signal is originating from the Ni-rich layers near the oxide-metal interface in which the Ni atoms probably have a magnetic moment close to the Ni bulk value. This assumption is corroborated by the finding of a strongly increasing magnetic moment with increasing Ni content in bulk nickel aluminum alloys. For an alloy composition of $Ni_{0.76}Al_{0.24}$ a magnetic moment 1.5 times as large as for Ni_3Al was found.[16,17]

IV. INDIVIDUAL Fe AND Co ADATOMS

In this section we present the magnetic properties of individual Fe and Co atoms on the $Al_2O_3/Ni_3Al(111)$ substrate. Both systems exhibit an out-of-plane easy magnetization axis and almost atomic like $r=L/(S+7D)$ values. We are not able to separately determine S and L because we miss the information if saturation is reached at the maximum available magnetic field (5 T) due to a rapidly changing XAS intensity with x-ray exposure hindering the acquisition of magnetization curves. The reason for this behavior will be outlined in Sec. IV B. We therefore prefer to give r and the branching ratio (BR), both being reliable numbers especially for not fully saturated samples. In the last Sec. IV C we discuss thermally activated adatom diffusion in order to highlight the influence of the small difference between the deposition and measuring temperature. We find that diffusion is active during deposition but suppressed at the measuring temperature and we elucidate the consequence on the abundance of single atoms at the surface and on the mean island size $\langle s \rangle$ as a function of time and temperature.

A. Chemical and magnetic properties

The XAS and XMCD spectra acquired for 0.03 ML $Fe/Al_2O_3/Ni_3Al(111)$ are shown in Figs. 3(b) and 3(c). The Fe L_3 and L_2 edges exhibit a pronounced multiplet structure typical for individual atoms having highly localized valence electrons and different from the spectra observed in bulk iron oxides.[23–26]

A characteristic feature determining the oxidation state of the Fe atoms is the r value introduced above. In bulk Fe oxides, Fe can be in a trivalent state (Fe_2O_3) corresponding to a $3d^5$ electronic configuration ($L=r=0$),[27] in a divalent state (FeO) equivalent to a $3d^6$ configuration ($L=1$; $r=0.26$) (Refs. 28 and 29) or in a mixed $\alpha 3d^5+\beta 3d^6$ state (Fe_3O_4) with intermediate value of $r<0.18$.[30,31] Any mixture of the three oxide stochiometries would therefore lead to $r<0.26$. For the surface adsorbed Fe atoms we obtain $r=0.53\pm0.09$ at $\theta=0°$ and $r=0.31\pm0.07$ at $\theta=70°$. This is distinctly different from iron oxide and indicative of the reduced symmetry and hybridization of the Fe atom on the alumina film giving rise to a large orbital moment. The fact that r is close to the free-atom value of 0.5 shows the effective decoupling of the Fe atoms from the metal substrate by the oxide film and the fact that r is distinctly different from any one of the iron oxides shows that Fe adatoms do not form an ionic bond to the oxygen in Al_2O_3 but rather adsorb

without much charge transfer on the pristine oxide.

The absence of oxidation is in agreement with the oxygen affinity to Al and Fe derived from the formation enthalpies of the respective oxides. The formation enthalpy of alumina is with 1675.7 kJ/mole much higher than the ones of Fe_3O_4 with 1118.4 kJ/mole, of Fe_2O_3 with 824.2 kJ/mole, and of FeO with 272.0 kJ/mole.[32] For the comparative oxygen affinity one has to scale these energies per mole O_2 for which one obtains 1117.1, 559.2, 549.5, and 544.0 kJ/mole of O_2, respectively. Therefore oxygen, once bound to Al, does not bind to Fe. On the other hand, oxygen bound in Fe_2O_3 strongly prefers to bind to Al once it is brought into contact with it. This is illustrated by the thermite reaction, where Al and Fe_2O_3 are heated to form Al_2O_3 and clean Fe. Due to the exothermity of this reaction the Fe melts and the reaction is used, e.g., for railroad welding.

Further evidence for the absence of oxide formation comes from the diffusion and nucleation behavior of Fe adatoms on $Al_2O_3/Ni_3Al(111)$.[9,13,15] By varying the deposition temperature one can either create two-dimensional or three-dimensional islands (160 vs 300 K) (Ref. 13) indicative of freely diffusing single metal atoms on an inert oxide support. Oxide formation is expected to lead to a strong directional bond pinning the atoms which would show up in STM images. However, the substrate between the Fe clusters is clean demonstrating that the Fe atoms are covalently chemisorbed on the atomically flat Al_2O_3 film.

From the integrated total XAS we obtain the branching ratio defined as

$$\mathrm{BR} = \frac{I(L_3)}{I(L_2)+I(L_3)} = \frac{\int_{L_3}(\mu_+ + \mu_-)dE}{\int_{L_2+L_3}(\mu_+ + \mu_-)dE}. \quad (1)$$

We find $\mathrm{BR}=0.82\pm0.03$ at 0° and 70°, suggesting a high-spin ground state for Fe.[33] Further, the large values of BR and r, suggest that the crystal-field splitting $10Dq$ has to be comparable with or smaller than the spin-orbit coupling constant ξ_{3d} of the $3d$ orbitals.[33] ξ_{3d} is between 50 meV and 100 meV for Fe and Co.[22] Assuming a small contribution from the $7D$ term to $(S+7D)$ the larger XMCD signal at the L_3 edge for $\theta=0°$ indicates an out-of-plane easy magnetization axis. The same easy magnetization axis is inferred for small Fe clusters from magnetization curves as outlined in Sec. V.

The XAS and XMCD spectra acquired on Co monomers are shown in Figs. 3(e) and 3(f). Again, these spectra have a pronounced multiplet structure and differ from the line shapes observed for Co^{3+} (Ref. 34) and Co^{2+} (Refs. 35 and 36) in the respective oxides. At 0° the L_3 dichroic signal has the same sign as the L_2 dichroic signal leading to an $L/(S+7D)$ ratio greater than $r=2/3$ which is obtained for absent L_2. We calculate $r=0.91\pm0.06$ for 0° and 0.68 ± 0.05 for 70°. The branching ratio is $\mathrm{BR}=0.89\pm0.03$ at 0° and 0.86 ± 0.03 at 70°. Also for Co, we infer an out-of-plane easy axis by comparing the $(\mu_+-\mu_-)$ signal at 0° and 70°, and as already discussed in case of Fe, we can assume a high-spin ground state and a crystal-field parameter similar to ξ_{3d}.

The absence of cobalt oxide formation can be discussed in a similar way as for Fe. The formation enthalpies are 891.0 kJ/mole for Co_3O_4,[32] 175.4 kJ/mole for Co_2O_3,[37] and 237.9 kJ/mole for CoO.[32] For the Co oxygen affinity one obtains 445.5, 116.9, and 475.8 kJ/mole per O_2, respectively, which is again smaller than the oxygen affinity of Al of 1117.1 kJ/mole of O_2. As for Fe we conclude that Co is adsorbed on the oxide but does not react with it.

When comparing the $(\mu_+ + \mu_-)$ signal taken at at 0° and 70° [see Fig. 3(e)], we find that they differ substantially. This is mainly a linear dichroism effect, i.e., an anisotropic spatial charge distribution of the d electrons, which can be proven by acquiring XAS with linearly polarized light. The electric field vector E_ν is oriented along the sample rotation axis and therefore lies in the sample plane independent of the angle θ; this direction has been labeled vertical (ν) in Fig. 3(a). Assuming isotropic in-plane chemical bonding or electric charge distribution the XAS with linear vertical polarization (μ_ν) is expected to have the same shape as the sum of the two XAS with circular polarization acquired at $\theta=0°$ $[(\mu_+ + \mu_-)_{0°}]$, which is a simple consequence of free basis choice.[15] We find indeed a very similar form for μ_ν and $(\mu_+ + \mu_-)_{0°}$ [see Figs. 3(d) and 3(e)] suggesting isotropic in-plane chemical bonding and charge distribution. This is reasonable when considering the finite size of the x-ray beam averaging over different domains of the Al_2O_3 film and over multiple adsorption sites. For $\theta=70°$, E_h mainly probes the out-of-plane d orbitals. The observed difference in the XAS measured with μ_h and μ_ν shows the significantly different in-plane and out-of-plane chemical bonding which is likely the origin of the observed MAE.

B. Beam induced change in the XAS white line

As mentioned earlier we observed a quickly changing XAS intensity as a function of the x-ray beam exposure time for single Fe and Co atoms. Yet, this intensity loss leaves the relative intensities in the different peaks and therefore the spectral shape unchanged. An example is shown in Fig. 4 for 0.02 ML Co on $Al_2O_3/Ni_3Al(111)$. Changes in the μ_+ absorption spectrum are more difficult to follow due to the small intensity compared with the μ_- signal. Therefore, we display in Fig. 4(a) a single μ_+ spectrum as a reference acquired at $t=900$ s and demonstrate the change over time in a series of μ_- spectra. The attenuation of some selected peaks is represented by the color coded dots in Fig. 4(b). The integrated μ_- $L_{2,3}$ intensity follows the solid line. When moving the x-ray beam over the sample to a new region, which has not been exposed before, the integrated $L_{2,3}$ peak intensity recovers to $(96\pm2)\%$ of the original value. The remaining difference can be attributed to sample inhomogeneity. Note that the change in the white line intensity is not reversible, as has been verified by temporarily switching off the x-ray beam and recording again a spectrum after 30 min.

Therefore the dramatic changes in the absorption and dichroism intensity are unequivocally induced by the x-ray beam. Aggregation due to beam induced surface diffusion can be excluded due to the fact that footprints of the spectral shape, such as r and BR stay constant, see Table I. Therefore

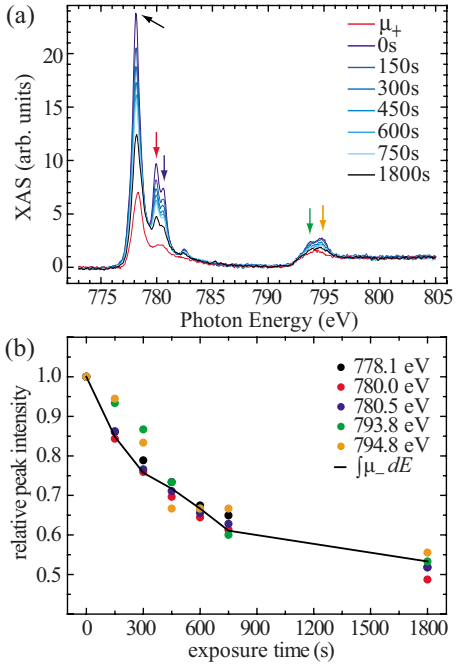

FIG. 4. (Color online) 0.02 ML $Co/Al_2O_3/Ni_3Al(111)$ (a) XAS taken at Co $L_{2,3}$ edges at $T=8$ K and $\mu_0 H=5$ T with positive (red line showing lowest intensity) and negative (blue lines) x-ray helicity for $\theta=0°$ as a function of the exposure time to the x-ray beam. (b) Evolution of the μ_- spectra's principal peaks marked with arrows in (a). The line represents the time dependence of the integrated μ_- absorption spectrum normalized to the $t=0$ s integral. The nonresonant transitions were subtracted.

the coordination of the metal atoms is constant excluding coarsening and the decrease in $\int_{L_2+L_3}(\mu_+ + \mu_-)$ with exposure time must be attributed to a decrease in the coverage which we explain by photon induced adatom desorption. We can express the desorption rate as

$$D = \sigma e \Theta A F_{ph}, \tag{2}$$

where σ is the x-ray absorption cross section, the efficiency e is the fraction of x-ray absorption events leading to desorption, Θ denotes the coverage, A the area of one adsorption site, and F_{ph} the photon flux. For Co the x-ray absorption

TABLE I. Ratio $r=L/(S+7D)$ and branching ratio BR $=I(L_3)/[I(L_2)+I(L_3)]$ as a function of the exposure time to the x-ray beam deduced from the spectra shown in Fig. 4.

Exposure time (s)	r	BR
0	0.92 ± 0.06	0.90 ± 0.03
150	0.90 ± 0.06	0.89 ± 0.03
300	0.91 ± 0.06	0.90 ± 0.03
450	0.95 ± 0.06	0.89 ± 0.03
600	0.96 ± 0.06	0.90 ± 0.03
750	0.99 ± 0.06	0.91 ± 0.03
1800	0.88 ± 0.06	0.91 ± 0.03

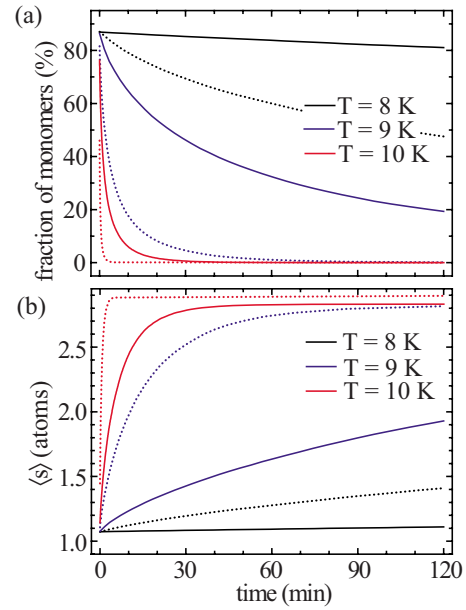

FIG. 5. (Color online) KMC simulation of the deposition of 0.02 ML with a flux of 10^{-3} ML/s on a hexagonal lattice and subsequent coarsening caused by monomer diffusion (attempt frequency $\nu_0=10^{13}$ s^{-1}) with $E_m=27$ meV (solid line) and $E_m=25$ meV (dotted line) at different temperatures. (a) Fraction of the coverage present in form of monomers as a function of time. (b) Mean island size $\langle s \rangle$ as a function of time. $t=0$ corresponds to the moment when deposition stops.

cross section is about $\sigma=10^{-2}$ photons^{-1} at the L_3 peak,[22] the photon flux is typically 10^{13} photons/(s mm^2),[38] and the area of one absorption site is $A=6\times10^{-14}$ mm^2. For $\Theta=0.02$ ML and $D=1.56\times10^{-4}$ s^{-1} this yields $e\simeq1$. Hence, each absorbed photon leads to the desorption of one Co atom.

C. Thermally activated adatom diffusion

Metal atoms on isolating surfaces are only weakly bound which often entails a migration barrier E_m much smaller than the ones of metal on metal systems.[39] For Co on h-BN we found a migration barrier of $E_m=23\pm3$ meV (Ref. 40) and for Au on a thin alumina film on NiAl(110) it was reported that the adatoms are immobile at $T=5$ K while they diffuse at $T\sim10$ K, which leads with an attempt frequency of 1×10^{13} Hz to 13 meV$\ll E_m \leq 26$ meV.[41] For the present system we observed a pronounced multiplet absorption spectrum (see Fig. 3) for Fe and Co which is typical for single atoms in covalent compounds[42] indicating that adatom diffusion and nucleation are suppressed at 8 K.

We performed kinetic Monte Carlo (KMC) simulations in order to estimate E_m and to quantify the effect of monomer diffusion on the abundance of single atoms and on the evolution of the mean island size $\langle s \rangle$ on our experimental time scale of about 2 h.[43] In Fig. 5 we present the results at three different temperatures and for two diffusion barriers. The minimum diffusion barrier needed to explain the frozen adatom diffusion at 8 K concluded from our observation of a strong multiplet structure is $E_m=27$ meV. On the other hand,

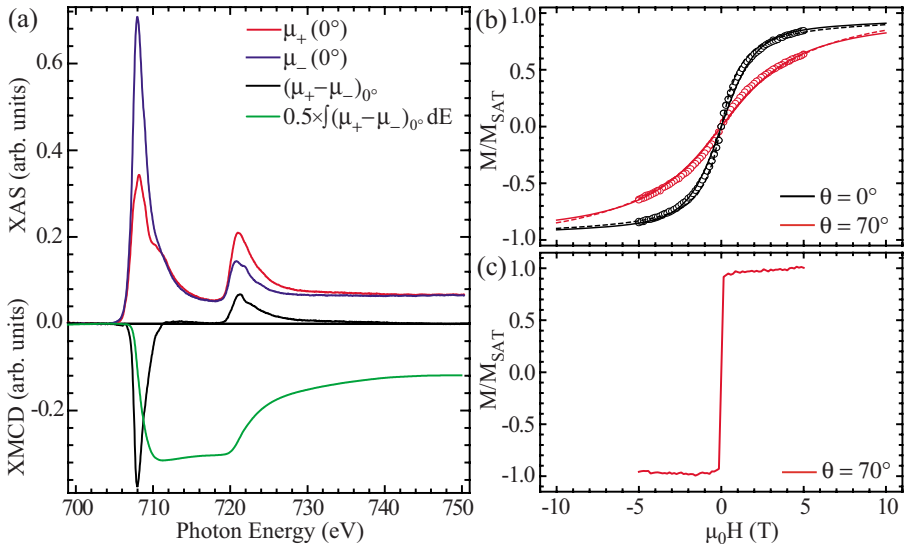

FIG. 6. (Color online) 0.14 ± 0.03 ML $Fe/Al_2O_3/Ni_3Al(111)$ deposited and measured at $T=8$ K. (a) XAS, resulting XMCD, and corresponding integral taken at Fe $L_{2,3}$ edges at $\mu_0 H=5$ T with right and left circularly polarized light for $\theta=0°$. (b) Fe magnetization curves (open circles) representing the peak of the L_3 XMCD intensity at 708.0 eV divided by the pre-edge intensity at 704.0 eV as a function of **H**. The solid and dashed lines are fits outlined in the text. (c) Ni magnetization curves representing the peak of the L_3 XMCD intensity at 853.1 eV divided by the pre-edge intensity at 849.8 eV as a function of **H**.

we find an upper bound very close to this value since we observe cluster formation for larger coverages at around 10 K as outlined in the next section. This defines E_m to 27 ± 1 meV under the assumption of an attempt frequency of $\nu_0 = 10^{13}$ Hz.

V. SMALL Fe CLUSTERS

For larger coverages we observe that the strong multiplet features of XAS and XMCD spectra vanish and the spectra look more like bulk Fe. This is attributed to cluster formation giving rise to hybridization among Fe atoms.[44] The XAS spectra taken on these clusters do not change over the investigation time of 2 h, which allows us to take XAS at 0° and 70°, as well as magnetization curves for Fe and for Ni. The data are presented in Fig. 6. From the shape of the magnetization curve shown in Fig. 6(b) we deduce an out-of-plane easy axis and remark that the magnetization is close to saturation at 0°. Note that this magnetization direction is opposite to the in-plane easy axis observed for large Co clusters grown on $Al_2O_3(0001)$.[45] The fact that saturation is achieved enables us to calculate the orbital and spin magnetic moment by means of the sum rules. With a typical value of $h_d=3.4$ for the number of d holes[44] we obtain $L=0.30 \pm 0.04 \mu_B$ and $S+7D=2.31 \pm 0.14 \mu_B$. The spin moment is large suggesting ferromagnetic alignment of the Fe moments among each other. Note that iron oxides often order ferrimagnetically or antiferromagnetically which is obviously not the case here.[26,46] This again supports the image of metallic Fe adsorbing on the largely inert oxide surface.

Interestingly, we find that the Fe clusters are magnetically decoupled from the ferromagnetic $Ni_3Al(111)$ substrate. This becomes evident from the different magnetization reversal observed in the magnetization curves shown in Figs. 6(b) and 6(c). The magnetization curve measured at the Fe edge has an s-shape saturating at fields >5 T whereas the one measured at the Ni edge has a square shape with a very small coercive field which cannot be resolved with the chosen field increments.

We determine the MAE of the Fe clusters from the magnetization loops. In the anisotropic superparamagnetic case, the energy of a particle of size s in an external magnetic field is given by the function $E(\theta, \vartheta, \varphi)$ composed of the Zeeman term $-sm\mu_0 H \cos \vartheta$ and, assuming uniaxial anisotropy, of the MAE term $-sK(\sin \theta \sin \vartheta \cos \varphi + \cos \vartheta \cos \vartheta)^2$. **H** is taken as the z axis, ϑ and φ are the polar and azimuthal coordinates of the magnetic moment **m** per atom, K is the magnetic anisotropy per atom, and θ defines the easy magnetization direction. The magnetization projected onto the magnetic field direction then reads[47]

$$M = M_{\mathrm{SAT}} \frac{\int_0^{2\pi} d\varphi \int_0^{\pi} d\vartheta \sin \vartheta \cos \varphi e^{-E(\theta,\vartheta,\varphi)/k_B T}}{\int_0^{2\pi} d\varphi \int_0^{\pi} d\vartheta \sin \vartheta e^{-E(\theta,\vartheta,\varphi)/k_B T}}. \quad (3)$$

From experiment we know the temperature T and the external field H. Because experimental information on the particle size s and size distribution are missing, we used again KMC simulations to gain further insight. In Table II the relative abundance of all cluster sizes up to $s=10$ is reported when depositing 0.14 ML at 10 K with a flux of 10^{-3} ML/s using $E_m=27$ meV and $\nu_0=10^{13}$ s^{-1}. Diffusion during deposition leads to aggregation and only a small amount of monomers remains when deposition stops. This is due to the long deposition time of 140 s and a relative high adatom density where diffusion by a few lattice sites suffices to form clusters. For comparison, when depositing 0.02 ML, where deposition

TABLE II. KMC simulations of Fe deposition with a flux of 10^{-3} ML/s using $E_m=27$ meV and $\nu_0=10^{13}$ s^{-1}. We present for two coverages $\Theta=0.02$ ML and 0.14 ML at $T=8$ K (statistic growth) and 10 K, the relative frequency of all cluster sizes up to $s=10$ and the mean cluster size $\langle s\rangle$.

Θ (ML)	T (K)	$s=1$ (%)	$s=2$ (%)	$s=3$ (%)	$s=4$ (%)	$s=5$ (%)	$s=6$ (%)	$s=7$ (%)	$s=8$ (%)	$s=9$ (%)	$s=10$ (%)	$\langle s\rangle$
0.14	8	36.4	23.3	14.9	9.4	5.9	3.7	2.4	1.5	0.9	0.6	1.73
0.14	10	7.0	13.4	16.1	15.3	12.9	10.0	7.4	5.2	3.7	2.6	3.33
0.02	8	86.9	11.4	1.5	0.2							1.07
0.02	10	76.4	19.6	3.4	0.5	0.1						1.14

takes only 20 s and the adatom density is low, 76.4% of all atoms are monomers [see also Fig. 5(a) at $t=0$]. The best fit of the hysteresis curves shown in Fig. 6(b) is obtained with $m=2.6\pm0.1\mu_B$/atom and $K=0.50\pm0.05$ meV/atom (solid line) when using the average cluster size $\langle s\rangle=3.33$. Note that the magnetic moment returned by the fitting procedure equals exactly the sum of the orbital moment and effective spin moment. An equally good fit (dashed line) can be obtained using the size distribution given by the KMC simulations for 0.14 ML deposited at 10 K with $m=2.2\pm0.1\mu_B$/atom and $K=0.60\pm0.05$ meV/atom assuming m and K independent of the cluster size. $K=0.5$ meV/atom is a surprisingly large MAE. For comparison, bulk bcc iron has an MAE of 2.4 μeV/atom (Ref. 48) and γ iron oxide of 1.5 μeV/Fe_2O_3.[49]

We note that the MAE is mainly an intrinsic property of the adsorbed Fe clusters and not due to dipolar coupling with the magnetic substrate. Using our measured magnetic moment of the substrate of $0.4\mu_B$/Ni atom and assuming a semi-infinite substrate yields a dipolar coupling <0.05 meV/Fe atom, which is an order of magnitude smaller than the MAE explaining our observation of magnetically decoupled Fe_3 clusters.

VI. CONCLUSION

The magnetic moments and magnetic anisotropy energies of single atoms and small clusters of Fe and Co deposited on $Al_2O_3/Ni_3Al(111)$ have been investigated by XAS with circular and linear polarized light. For isolated Fe and Co atoms we found very large values of the ratio $r=L/(S+7D)$ which translate into large orbital moments. The data give $r=0.53\pm0.09$ for Fe and $r=0.91\pm0.06$ for Co, very close to the free-atom values of $r=0.5$ for $3d^6$ (Fe) and $r=1$ for $3d^7$ (Co). The comparison of the hysteresis curves acquired at the Fe and Ni edges allows to exclude any dipolar or exchange coupling between the transition-metal nanostructures and the substrate. Both these findings demonstrate that the the ultrathin alumina film produces an effective decoupling of the magnetic atoms from the conduction electrons of the underlying metal. We demonstrated by means of measurements with linearly polarized x rays that the out-of-plane easy magnetization axis for Fe and Co is due to the formation of a highly directional electronic bonding between the $3d$ states of Fe (Co) and the $2p$ states of the oxygen terminated Al_2O_3 surface.

[1] P. Gambardella, S. Rusponi, M. Veronese, S. S. Dhesi, C. Grazioli, A. Dallmeyer, I. Cabria, R. Zeller, P. H. Dederichs, K. Kern, C. Carbone, and H. Brune, Science **300**, 1130 (2003).
[2] P. Gambardella, S. S. Dhesi, S. Gardonio, C. Grazioli, P. Ohresser, and C. Carbone, Phys. Rev. Lett. **88**, 047202 (2002).
[3] C. F. Hirjibehedin, C. P. Lutz, and A. J. Heinrich, Science **312**, 1021 (2006).
[4] C. F. Hirjibehedin, C.-Y. Lin, A. F. Otte, M. Ternes, C. P. Lutz, B. A. Jones, and A. J. Heinrich, Science **317**, 1199 (2007).
[5] A. F. Otte, M. Ternes, K. von Bergmann, S. Loth, H. Brune, C. P. Lutz, C. F. Hirjibehedin, and A. J. Heinrich, Nat. Phys. **4**, 847 (2008).
[6] H. Brune and P. Gambardella, Surf. Sci. **603**, 1812 (2009).
[7] U. Bardi, A. Atrei, and G. Rovida, Surf. Sci. **239**, L511 (1990).
[8] U. Bardi, A. Atrei, and G. Rovida, Surf. Sci. **268**, 87 (1992).
[9] M. Schmid, G. Kresse, A. Buchsbaum, E. Napetschnig, S. Gritschneder, M. Reichling, and P. Varga, Phys. Rev. Lett. **99**, 196104 (2007).
[10] A. Rosenhahn, J. Schneider, J. Kandler, C. Becker, and K. Wandelt, Surf. Sci. **433-435**, 705 (1999).
[11] C. Becker, J. Kandler, H. Raaf, R. Linke, T. Pelster, M. Dräger, M. Tanemura, and K. Wandelt, J. Vac. Sci. Technol. A **16**, 1000 (1998).
[12] S. Gritschneder, S. Degen, C. Becker, K. Wandelt, and M. Reichling, Phys. Rev. B **76**, 014123 (2007).
[13] A. Lehnert, A. Krupski, S. Degen, K. Franke, R. Decker, S. Rusponi, M. Kralj, C. Becker, H. Brune, and K. Wandelt, Surf. Sci. **600**, 1804 (2006).
[14] S. Degen, A. Krupski, M. Kralj, A. Langner, C. Becker, M. Sokolowski, and K. Wandelt, Surf. Sci. **576**, L57 (2005).
[15] T. Maroutian, S. Degen, C. Becker, K. Wandelt, and R. Berndt, Phys. Rev. B **68**, 155414 (2003).
[16] F. R. de Boer, C. J. Schinkel, J. Biesterbos, and S. Proost, J. Appl. Phys. **40**, 1049 (1969).
[17] S. K. Dhar, K. A. Gschneidner, L. L. Miller, and D. C. Johnston, Phys. Rev. B **40**, 11488 (1989).
[18] B. T. Thole, P. Carra, F. Sette, and G. van der Laan, Phys. Rev. Lett. **68**, 1943 (1992).

[19] P. Carra, B. T. Thole, M. Altarelli, and X. Wang, Phys. Rev. Lett. **70**, 694 (1993).
[20] G. Moulas, A. Lehnert, S. Rusponi, J. Zabloudil, C. Etz, S. Ouazi, M. Etzkorn, P. Bencok, P. Gambardella, P. Weinberger, and H. Brune, Phys. Rev. B **78**, 214424 (2008).
[21] R. Wu and A. J. Freeman, Phys. Rev. Lett. **73**, 1994 (1994).
[22] J. Stöhr and H. Siegmann, *Magnetism—From Fundamentals to Nanoscale Dynamics* (Springer, Heidelberg, 2006).
[23] H.-J. Kim, J.-H. Park, and E. Vescovo, Phys. Rev. B **61**, 15284 (2000).
[24] J. Chen, D. J. Huang, A. Tanaka, C. F. Chang, S. C. Chung, W. B. Wu, and C. T. Chen, Phys. Rev. B **69**, 085107 (2004).
[25] C. I. Pearce, C. M. B. Henderson, R. A. D. Pattrick, G. van der Laan, and D. J. Vaughan, Am. Mineral. **91**, 880 (2006).
[26] J.-Y. Kim, T. Y. Koo, and J.-H. Park, Phys. Rev. Lett. **96**, 047205 (2006).
[27] F. M. F. de Groot, P. Glatzel, U. Bergmann, P. A. van Aken, R. A. Barrea, S. Klemme, M. Hävecker, A. Knop-Gericke, W. M. Heijboer, and B. M. Weckhuysen, J. Phys. Chem. B **109**, 20751 (2005).
[28] R. J. Radwanski and Z. Ropka, Physica B **403**, 1453 (2008).
[29] A. Svane and O. Gunnarsson, Phys. Rev. Lett. **65**, 1148 (1990).
[30] D. J. Huang, C. F. Chang, H.-T. Jeng, G. Y. Guo, H.-J. Lin, W. B. Wu, H. C. Ku, A. Fujimori, Y. Takahashi, and C. T. Chen, Phys. Rev. Lett. **93**, 077204 (2004).
[31] E. Goering, S. Gold, M. Lafkioti, and G. Schutz, Europhys. Lett. **73**, 97 (2006).
[32] *CRC Handbook of Chemistry and Physics*, 89th ed., edited by D. R. Lide (CRC Press/Taylor & Francis, Cleveland/London, 2009).
[33] B. T. Thole and G. van der Laan, Phys. Rev. B **38**, 3158 (1988).
[34] F. M. F. de Groot and A. Kotani, *Corel Level Spectroscopy of Solids*, Advances in Condensed Matter Science Vol. 6 (CRC Press, Cleveland, 2008).
[35] S. I. Csiszar, M. W. Haverkort, Z. Hu, A. Tanaka, H. H. Hsieh, H.-J. Lin, C. T. Chen, T. Hibma, and L. H. Tjeng, Phys. Rev. Lett. **95**, 187205 (2005).
[36] F. M. F. de Groot, M. Abbate, J. van Elp, G. A. Sawatzky, Y. J. Ma, C. T. Chen, and F. Sette, J. Phys.: Condens. Matter **5**, 2277 (1993).
[37] Y. Idemoto and T. Matsui, Solid State Ionics **179**, 625 (2008).
[38] O. Renault, N. Barrett, A. Bailly, L. Zagonel, D. Mariolle, J. Cezar, N. Brookes, K. Winkler, B. Krömker, and D. Funnemann, Surf. Sci. **601**, 4727 (2007).
[39] H. Brune, Surf. Sci. Rep. **31**, 121 (1998).
[40] P. Buluschek, Ph.D. thesis, Ecole Polytechnique Fédérale de Lausanne, 2007.
[41] M. Kulawik, N. Nilius, and H.-J. Freund, Phys. Rev. Lett. **96**, 036103 (2006).
[42] G. van der Laan and B. T. Thole, Phys. Rev. B **43**, 13401 (1991).
[43] We use a KMC code based on the one used in Ref. 50 and described in Ref. 39. The code hase been improved by M. El Ouali and P. Buluschek. It treats a hexagonally close-packed surface and allows only the occupation of fcc sites. For the present purpose, we assume that the dimer is stable and neglect desorption and edge or corner diffusion.
[44] C. T. Chen, Y. U. Idzerda, H.-J. Lin, N. V. Smith, G. Meigs, E. Chaban, G. H. Ho, E. Pellegrin, and F. Sette, Phys. Rev. Lett. **75**, 152 (1995).
[45] T. Hill, S. Stempel, T. Risse, M. Bäumer, and H. J. Freund, J. Magn. Magn. Mater. **198-199**, 354 (1999).
[46] H. Shiroishi, T. Oda, I. Hamada, and N. Fujima, Eur. Phys. J. D **24**, 85 (2003).
[47] P. Gambardella, A. Dallmeyer, K. Maiti, M. C. Malagoli, W. Eberhardt, K. Kern, and C. Carbone, Nature (London) **416**, 301 (2002).
[48] K. Honda, S. Kaya, and Y. Masuyama, Nature (London) **117**, 753 (1926).
[49] J. B. Birks, Proc. Phys. Soc. London, Sect. B **63**, 65 (1950).
[50] J. Jacobsen, K. W. Jacobsen, P. Stoltze, and J. K. Nørskov, Phys. Rev. Lett. **74**, 2295 (1995).
[51] A. Lehnert, Ph.D. thesis, Ecole Polytechnique Fédérale de Lausanne, 2009.